

ALLO: A Photorealistic Dataset and Data Generation Pipeline for Anomaly Detection During Robotic Proximity Operations in Lunar Orbit

Selina Leveugle¹, Chang Won Lee², Svetlana Stolpner³, Chris Langley³,
Paul Grouchy³, Steven Waslander², and Jonathan Kelly¹

Abstract—NASA’s forthcoming Lunar Gateway space station, which will be uncrewed most of the time, will need to operate with an unprecedented level of autonomy. Enhancing autonomy on the Gateway presents several unique challenges, one of which is to equip the Canadarm3, the Gateway’s external robotic system, with the capability to perform worksite monitoring. Monitoring will involve using the arm’s inspection cameras to detect any anomalies within the operating environment, a task complicated by the widely-varying lighting conditions in space. In this paper, we introduce the visual anomaly detection and localization task for space applications and establish a benchmark with our novel synthetic dataset called ALLO (for Anomaly Localization in Lunar Orbit). We develop a complete data generation pipeline to create ALLO, which we use to evaluate the performance of state-of-the-art visual anomaly detection algorithms. Given the low tolerance for risk during space operations and the lack of relevant data, we emphasize the need for novel, robust, and accurate anomaly detection methods to handle the challenging visual conditions found in lunar orbit and beyond.

I. INTRODUCTION

Over the past two decades, the international space community has begun to focus its efforts on extending human space exploration beyond low-Earth orbit. NASA’s Artemis program, for example, aims to deploy the Lunar Gateway, the first space station in lunar orbit, that will test new technologies needed for extended deep-space missions [1]. Unlike the International Space Station (ISS), the Gateway will be required to operate autonomously and without an on-board crew for long periods. Its distance from the Earth and its orbit will hinder rapid and stable communication for control [2]. Autonomy is especially vital for the Canadarm3, the external robotic system under development by MDA Space Ltd. and the Canadian Space Agency, which will play a multifaceted role on the Gateway, including station maintenance, inspection, and the capture of visiting vehicles [3].

Solutions that utilize the arm’s cameras to autonomously detect potential collision hazards, such as loose tools or debris, are of particular interest, as they would significantly reduce the risk of damage to the arm during autonomous



Fig. 1: Blender rendering of the ISS model used in the ALLO dataset as a surrogate for the Lunar Gateway. The Earth, the Moon, and the Sun are shown in the background; reference camera positions around the station are highlighted in orange.

operations. Since the type and appearance of all possible hazards cannot be known in advance, it is beneficial for the vision system to perform *anomaly detection*, recognizing any off-nominal situations that are different from expected norms.

Anomaly detection and localization involves identifying and pinpointing the locations of unexpected content in images that deviate from a set of expected inputs. Algorithms for anomaly detection aim to find pixels, features, or objects in an image that differ statistically from an established baseline [4]. Anomaly detection in the space domain is challenging due to complex lighting conditions that result from the black background coupled with harsh direct solar illumination. Furthermore, the varied camera viewpoints used during robotic operations on a space station can cause anomalies to blend in with the background, making anomaly detection more difficult.

Although reliable anomaly detection is highly valuable to prevent the Canadarm3 from collisions, current methods do not directly address this task. Moreover, existing space image datasets from on-orbit operations, such as those from the Canadarm2 on the ISS, are limited and insufficient for developing an anomaly detection algorithm for the Canadarm3. Images from past missions lack ground truth reference and generally cannot be applied to operations in lunar orbit. To bridge this gap, we create an open-source anomaly detection dataset for robotic operations on an orbital space station and use it to evaluate state-of-the-art anomaly detection algorithms. To this end, our main contributions are as follows.

¹Space and Terrestrial Autonomous Robotic Systems (STARS) Laboratory at the University of Toronto Institute for Aerospace Studies (UTIAS), Toronto, Canada. Email: <firstname>.<lastname>@robotics.utias.utoronto.ca

²Toronto Robotics and AI Laboratory (TRAIL) at the University of Toronto Institute for Aerospace Studies (UTIAS), Toronto, Canada. Email: john.lee@robotics.utias.utoronto.ca; steven.waslander@robotics.utias.utoronto.ca

³MDA Space Inc. Email: <firstname>.<lastname>@mda.space

- We present a new and relevant visual anomaly detection task that goes beyond standard terrestrial applications.
- We develop a simulator and automated data generation pipeline, which makes use of Blender’s Cycles rendering engine.
- We introduce the ALLO (Anomaly Localization in Lunar Orbit) dataset, an open-source dataset for anomaly detection as part of vision-based proximity operations for space-based robotic systems. The dataset comprises 94,890 anomaly-free images and 17,527 anomalous images with pixel-level ground-truth maps.
- We establish a new anomaly detection benchmark by evaluating existing anomaly detection algorithms on the ALLO dataset, and discuss how the existing methods are insufficient for the space domain.
- We validate the fidelity of the rendering process by reconstructing images captured from Earth orbit by ISS cameras and comparing them to existing images.

The remainder of this paper is structured as follows. Section II reviews anomaly detection datasets and algorithms. Section III details the simulation and rendering of the ALLO dataset. Section IV evaluates state-of-the-art anomaly detection algorithms on the ALLO dataset. The ALLO dataset and the data generation pipeline and benchmarking code are available at <https://github.com/utiasSTARS/ALLO.git>.

II. RELATED WORK

Although anomaly detection has not yet been applied to the space domain, extensive literature exists on vision-based navigation datasets for space exploration and, separately, on anomaly detection for industrial inspection. In this section, we review existing visual datasets for space missions and current approaches to anomaly detection.

A. Datasets for Anomaly Detection and Space Operations

a) Space Operations: In space exploration, visual navigation datasets are often generated using computer rendering software. Existing data from past missions are usually unsuitable for algorithm development since the images may be inapplicable to new missions, lack ground truth references, or have incorrect sensor configurations. Additionally, acquiring new images may be impossible, as in the case of the Gateway, or inadequate, due to limitations regarding what can be replicated on Earth [5]. Therefore, rendering programs are used to make synthetic space image datasets [5]–[10] as this allows an extensive range of scenarios to be realistically created. Rendering programs use engines such as Cycles [11] or Unreal Engine 5 [12] to accurately replicate the scenes they expect to encounter during their respective missions. Unlike existing space datasets, the ALLO dataset contains images of a space station in lunar orbit and is open source.

b) Industrial Defect Inspection: Recent advances in anomaly detection have focused on finding manufacturing defects during industrial inspection. The MVTEC 2D anomaly detection dataset [13] is the most widely used benchmark for this application due to its pixel-level annotations and diverse range of objects/textures [14]. However, like other anomaly

detection datasets such as BTech [15] and Kolektor [16], MVTEC features static viewpoints, consistent lighting, and simple backgrounds. In contrast, the ALLO dataset offers a more comprehensive and diverse set of scenes for space anomaly detection, including multiple views of the ISS with varied lighting conditions and backgrounds. This diversity sets ALLO apart from these other datasets, providing a broader range of scenarios for anomaly detection in space.

B. Anomaly Detection Methods

Anomaly detection involves identifying abnormal samples that deviate from the expected distribution [17]. Generally, an anomaly can be described as an irregular or unexpected instance that deviates from an established pattern [18]. Differentiating between normal and anomalous instances can be challenging due to two key issues [19]:

- Anomaly uncertainty: it is usually not known in advance what an anomaly might look like.
- Anomaly scarcity: anomalies are rare and diverse, making it difficult to identify all of them correctly.

To tackle these challenges, many anomaly detection algorithms have leveraged deep learning techniques [18]. Most methods are unsupervised because of the absence of representative anomalous data for supervision, though self-supervised methods also exist. Unsupervised methods [20]–[22] learn from anomaly-free images and classify anomalies based on deviations from this learned distribution, while self-supervised methods [23], [24] add synthetic anomalies to normal images during training. Overall, learned anomaly detection algorithms fall into two categories: representation-based and reconstruction-based methods.

1) Representation-based methods: Representation-based methods leverage embeddings from pre-trained feature extractors, such as ResNet [25] or ViT [26], combined with an outlier detection framework [27]. PaDiM [20] uses a pre-trained CNN to create a bag-of-features, reduces dimensions through random selection, fits a multivariate Gaussian distribution to each patch embedding, and detects anomalies based on the Mahalanobis distance between a test feature and the learned distribution [27]. Similarly, DFM [28] employs a bag-of-features approach but uses PCA for dimensionality reduction and fits a Gaussian mixture model to normal features, identifying anomalies via log-likelihood. Alternatively, PatchCore [27] and CFA [22] use memory banks to store normal features, scoring anomalies based on the distance between test features and stored features. PatchCore uses an ImageNet pre-trained network for patch-level storage, whereas CFA applies transfer learning to the target dataset to learn high-probability features.

Some representation methods use normalizing flows that learn an invertible mapping between the input features and a known reference distribution (eg. Multivariate Gaussian distribution) [29] [30] [31]. For instance, CFLOW-AD [32] uses a pre-trained feature extractor to extract feature maps from image patches, then learns a conditional normalizing flow that maps these vectors to a multivariate Gaussian distribution, calculating anomaly scores via the Mahalanobis

distance. FastFlow [33] extends this idea to two dimensions to preserve spatial information, and classifies anomalies based on feature likelihood. U-Flow [26] employs a U-net architecture where the encoder is a feature extractor and the decoder is a normalizing flow model, and anomalies are scored based on feature likelihood and the number of false alarms.

2) *Reconstruction-based methods*: Reconstruction-based anomaly detection methods use generative models to learn how to reconstruct only anomaly-free images. These methods operate on the assumption that anomalous features will be incorrectly reconstructed as they were not seen during training [14]. Possible types of image generators include generative adversarial networks (GANs) [34] [35], auto-encoders [36] [37], and student-teacher models [38] [21].

Student-teacher methods use knowledge distillation to train a student network to reconstruct anomaly-free images. Architectures differ between methods: STFPM [38] employs identical architectures for both the student and teacher networks, whereas Reverse Distillation [21] uses a mirrored architecture, where the student network is a reversed version of the teacher network. GAN-based reconstruction methods adversarially train an auto-encoder to reconstruct only normal images [39]. Ganomaly [34] uses encoder-decoder-encoder sub-networks and classifies the latent space representation of the reconstructed image with a discriminator. Both DRAEM [23] and DSR [40] generate synthetic anomalies by adding noise to the normal images to enhance robustness.

III. DATASET DESCRIPTION

The images captured by Canadarm3 are expected to contain diverse lighting conditions resulting from the combination of the black background of space, direct sunlight, indirect reflections from the Moon or station, and the arm’s inspection lights. Blender was chosen to create the ALLO dataset and replicate these lighting conditions because its Cycles rendering engine uses path tracing to calculate highly realistic lighting.

A. Blender Model Setup

Images of the Gateway’s orbit around the Moon were created using NASA’s model of the ISS [41] because a realistic Gateway model is not yet available. The ISS model’s textures and structure are representative of what the Canadarm3’s cameras will capture, as the Gateway is expected to resemble the ISS in appearance. The Gateway’s orbit [42] was approximated in Blender with an ellipse whose dimensions matched the perilune and apolune of the station’s orbit. Then, the positions of the Earth and Sun relative to the Moon were calculated with the Skyfield library [43] using ephemeris data

Dataset Set	Training	Test	Total
Camera Poses	1-40	41-50	50
Normal Images	87,600	7,290	94,890
Anomalous Images	0	17,527	17,527

TABLE I: Number of images in the ALLO dataset.

from the year 2030. The positions of the Moon, Earth, and Sun relative to the station were simulated over 365 days, replicating the lighting and background conditions the arm’s cameras will experience during operation.

In the Blender model, 50 unique camera poses were manually defined around the station to simulate key positions of the arm-mounted cameras. During the rendering process, random Gaussian noise was added to each pose, with a standard deviation of 1 meter for location and 0.2 radians in roll, pitch, and yaw. This process ensured that all relevant regions of the station body were captured and varied between views. The station model and some of the reference camera positions are shown in Fig. 1. Furthermore, to enhance the dataset’s generalizability, several scene parameters were modified during the rendering process. Each scene was rendered multiple times with varying sun strength intensities, which were carefully adjusted to achieve the desired effect. Each anomalous scene was also rendered with the anomaly at three different depths: the initial randomly assigned depth, as well as 1 metre closer to and 1 metre farther from the camera, resulting in a total of nine images for each anomalous scene. Furthermore, the anomaly’s size in each scene was randomly varied to one of three scales: its original size, 20% smaller, or 20% larger, to introduce additional diversity.

Algorithm 1 ALLO Dataset Rendering Process

```

1: for day in ephemeris data do
2:   Position the Moon, Earth, and Sun
3:   if Anomalous then
4:     CameraList = Cameras 40-49
5:   else if Normal then
6:     CameraList = Cameras 0-39
7:   end if
8:   for Camera in CameraList do
9:     for Set of sun light and anomaly parameters do
10:      Place a camera with slight pose perturbation
11:      Add a spotlight near the camera
12:      if Anomalous then
13:        while Anomaly < 0.1% of Image do
14:          Add anomaly inside camera frustum
15:        end while
16:      Render three-class segmentation mask
17:    end if
18:    Render the image using Cycles
19:    Add noise and glare
20:  end for
21: end for
22: end for

```

B. Image Rendering

The normal and anomalous images were generated from different camera positions to ensure variation between the training and testing sets. Models of thermal blankets, cables, and maintenance tools, such as those shown in Fig. 3, were used as anomalies. Each anomalous image contained only one anomaly, as performance on a single anomaly reflects

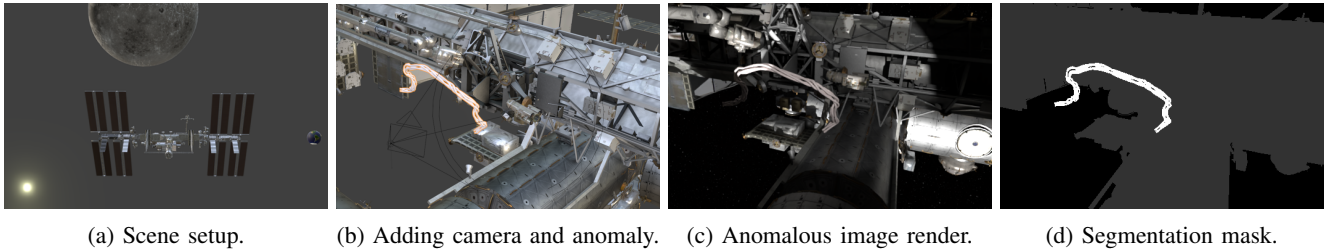


Fig. 2: Rendering process for an anomalous image in the ALLO dataset. The setup of the station and celestial bodies are shown in 2a, the placement of the camera and anomalous cable are shown in 2b, and the rendered anomalous image and the corresponding segmentation mask are presented in 2c and 2d respectively.

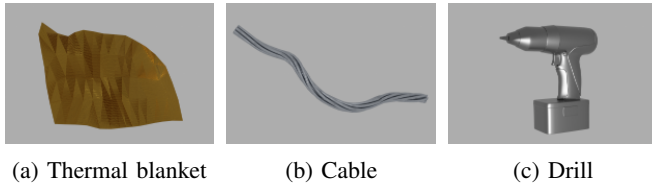


Fig. 3: Examples of models of anomalous objects used in the ALLO dataset.

how algorithms would perform on images with multiple anomalies. For all images, a corresponding three-class segmentation mask was generated that labelled the anomaly (none if normal image), all non-anomalous foreground objects (e.g., the station, celestial bodies), and the background (e.g. space). The rendering process for the ALLO dataset is outlined in Algorithm 1, with an example shown in Fig. 2.

All images in the ALLO dataset were rendered to a resolution of $1,920 \times 1,080$ pixels. The rendering process was repeated with two seeds and the breakdown of images in the training and testing sets are shown in Table I. Sample images from the ALLO dataset are shown in Fig. 4 and demonstrate how these images can be quite crowded, may contain both illuminated and shadowed structures, and have large black portions of space.

C. Dataset Validation

We demonstrate that our synthetic images accurately represent the scenes expected to be captured by the Canadarm3 by replicating real ISS images using the Blender model. Two pairs of replicated images are shown in Fig. 5, showing that both the lighting and textures of the scene are well captured by the Blender model. Seven replica images were compared to real ISS images using the Structural Similarity Index Measure (SSIM) [44]. While the average SSIM score was 0.32 due to illumination differences caused by the station’s colour, ALLO images are visually similar to real ISS images.

IV. EXPERIMENTS

Current approaches to anomaly detection have not yet been applied to the space domain. Therefore, we use the ALLO dataset to evaluate how state-of-the-art anomaly detection algorithms perform on more challenging imagery.

A. Experimental Setup

We used Intel’s Anomalib repository [45] to test state-of-the-art anomaly detection algorithms on the ALLO dataset. Anomalib was selected because it supports a large number of algorithms and because it enables the comprehensive testing and tuning of these algorithms on our data. We modified the Anomalib code to load and train on the ALLO dataset, and the following seven algorithms were evaluated: STFPM [38], CFA [22], Reverse Distillation [21], DRAEM [23], FastFlow [33], U-Flow [26], and DSR [40]. The MVTEC dataset results for the evaluated algorithms are presented in Table III. It should be noted that representation-based methods, which rely on discriminative image features, usually use fixed pre-trained encoders, often trained on ImageNet [46], while training the remaining network layers from scratch on the target dataset.

Each algorithm was first trained with its default hyperparameters. Then, the mean and standard deviation values of the ALLO training set were computed for image normalization unlike previous works that use ImageNet values. Additionally, horizontal and vertical flipping, as well as random brightness and contrast augmentations, were applied randomly with a 50% probability during training.

B. Evaluation Metrics

Three metrics were used to evaluate anomaly detection algorithms on the ALLO dataset: image AUROC (I.AUROC), pixel AUROC (P.AUROC), and average precision (P.AP). Image AUROC and pixel AUROC (area under receiver operating characteristic) were chosen for their effectiveness in assessing binary classifiers [26], but pixel AUROC can be misleading. A high pixel AUROC often reflects a strong true negative rate, particularly for small anomalies, indicating better detection of normal pixels rather than anomalies. A low score suggests difficulty with normal pixels due to a high false positive rate, with random classifiers scoring 0.5. Average precision (AP), which considers both precision and recall, better assesses pixel-level localization, especially for imbalanced datasets [28], [32]. Due to the heavy class imbalance between anomalous and non-anomalous pixels in ALLO test images, the best-performing algorithm was primarily determined by the highest pixel AP. However, pixel AUROC was also given consideration, as a low score indicates a high false positive rate, which is critical in evaluating anomaly detection performance.

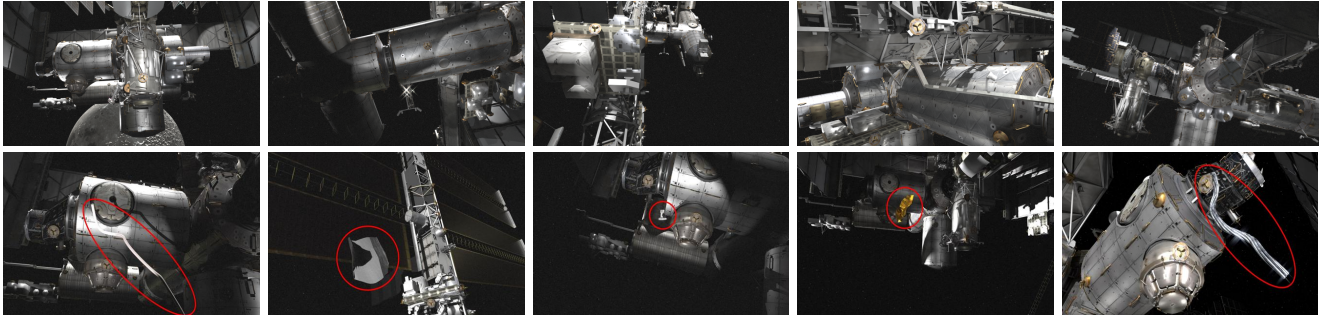


Fig. 4: Sample images from the ALLO dataset. Normal (anomaly-free) images are shown in the top row and anomalous images in the bottom row with the anomalies circled in red.

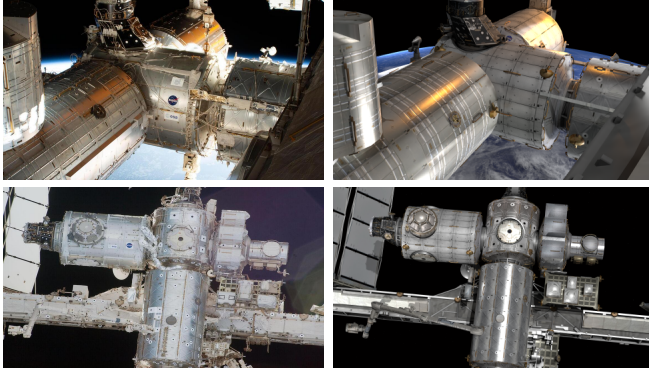


Fig. 5: Images taken by the ISS (left) and their synthetic recreations (right).

C. Results

The results of all algorithms on the ALLO test set are shown in Table III. Reverse Distillation (Rev. Dist.) achieved the highest pixel AP at 48.4%, followed by STFPM at 32.4% and FastFlow at 31.7%. Compared to its performance on the MVTec dataset, Reverse Distillation’s image AUROC score decreased by 40.4%, and its pixel AUROC dropped by 46.0% on the ALLO dataset. While Reverse Distillation had the highest pixel AP score, it had a fairly low pixel AUROC score indicating a high false positive rate. FastFlow had the highest image and pixel AUROC scores at 66.9% and 86.0% respectively. Generally, the student-teacher methods (STFPM and Rev. Dist.) performed best, followed by the normalizing flow methods (FastFlow and UFlow), while the semi-supervised methods (DRAEM and DSR) performed worse. Example inferences are shown in Fig. 6.

D. Ablation Studies

While all algorithms struggled to generalize to the space domain, we improved the performance of most algorithms using dataset-specific tuning, described in Section IV-A. The effect of data augmentation and custom normalization on FastFlow (the algorithm with the highest pixel AUROC) is shown in Table II. FastFlow was able to achieve higher pixel AUROC and pixel AP scores when using custom image statistics than with ImageNet-based normalization values. This reflects how different the scenes in the ALLO dataset are to those in ImageNet and other datasets that use ImageNet normalization values.

Due to the significant performance drop on the ALLO dataset compared to the MVTec dataset, we tested the algorithms on more visually distinct anomalies. We created a smaller, secondary test set where the anomalies’ colours were altered from their default colours (which usually resemble the station) to more distinct colours (e.g. red, blue, yellow). This experiment helped to determine how much the algorithms depend on the visual characteristics of anomalies. The results on the coloured test set are shown in Table IV and inference examples are visualized in Fig. 7; all algorithms showed a significant increase in performance. UFlow achieved the highest pixel AP score of 91.7%, representing a 63.3% increase over its performance on the primary test set. FastFlow recorded the best image AUROC score at 98.8% and the highest pixel AUROC score at 99.4%, showing 31.9% and 13.4% improvements, respectively.

E. Discussion

Our results in Section IV-C show that existing anomaly detection algorithms are ill-suited for the space domain. They assume commonly seen features such as those found in ImageNet, [27] which are not found in ALLO. Without adapting to the ALLO dataset, the feature extraction networks pre-trained on ImageNet extract non-discriminative feature representations, which hinders the ability of anomaly detection algorithms to effectively learn the dataset’s distribution

Some algorithms assume features will follow a uni-modal distribution [20] [33] of anomaly-free features. This assumption can be problematic for diverse datasets where anomalies have subtle features close to the normal distribution or when the normal data is multi-modal [23]. The handling of a more complex distribution is why the normalizing flow method FastFlow detects anomalies well without introducing too many false positives. As shown by the examples in Fig. 6, even the best-performing algorithms struggled to find anomalies whose colour resembled that of the station.

The most significant limitation of existing anomaly de-

Augmentations	I.AUROC \uparrow	P.AUROC \uparrow	P.AP \uparrow
MVTec	67.6 \pm 0.7	81.5 \pm 1.3	21.8 \pm 2.3
ALLO	66.9 \pm 2.3	86.0 \pm 2.8	31.7 \pm 1.2

TABLE II: The effect of tuned augmentations and normalization on FastFlow’s performance on the ALLO test set.

Dataset	Model	FastFlow [33]	UFlow [26]	CFA [22]	DRAEM [23]	DSR [40]	Rev. Dist. [21]	STFPM [38]
MVTec	Image AUROC \uparrow	<u>99.4</u>	98.9	99.5	98.0	98.2	98.5	95.5
	Pixel AUROC \uparrow	<u>98.5</u>	98.7	<u>98.5</u>	97.3	-	97.8	97.0
	Pixel AP \uparrow	-	-	-	68.4	70.2	-	-
ALLO	Image AUROC \uparrow	66.9 \pm 2.3	65.5 \pm 1.2	58.6 \pm 0.4	55.9 \pm 3.4	53.9 \pm 2.0	58.1 \pm 0.7	63.1 \pm 0.9
	Pixel AUROC \uparrow	86.0 \pm 2.8	85.6 \pm 0.7	85.1 \pm 0.5	67.9 \pm 1.2	55.4 \pm 1.0	51.8 \pm 0.0	58.1 \pm 6.4
	Pixel AP \uparrow	31.7 \pm 1.2	<u>28.4 \pm 1.8</u>	16.3 \pm 1.0	9.4 \pm 2.6	26.9 \pm 3.6	48.4 \pm 0.7	<u>32.4 \pm 12.6</u>

TABLE III: Performance of state-of-the-art anomaly detection algorithms on the ALLO and MVTec test sets. For each metric, the algorithm that performed best and second-best on that dataset are bolded and underlined, respectively.

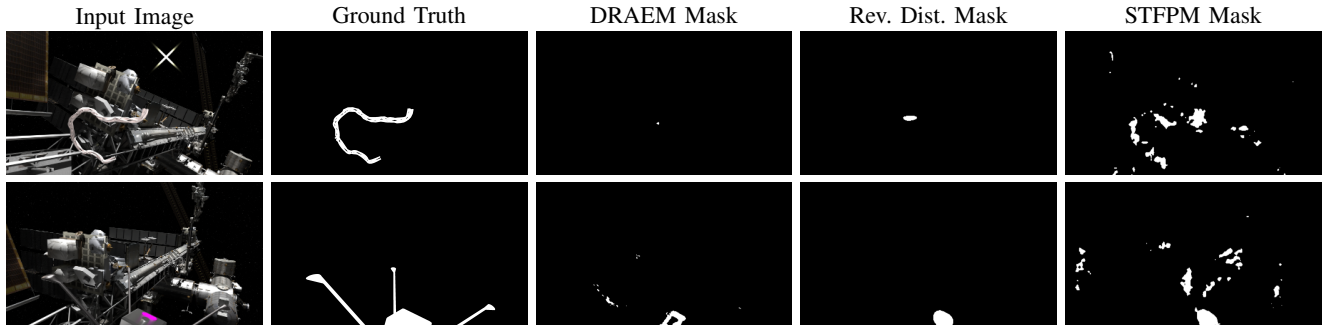


Fig. 6: Example predictions from anomaly detection algorithms.

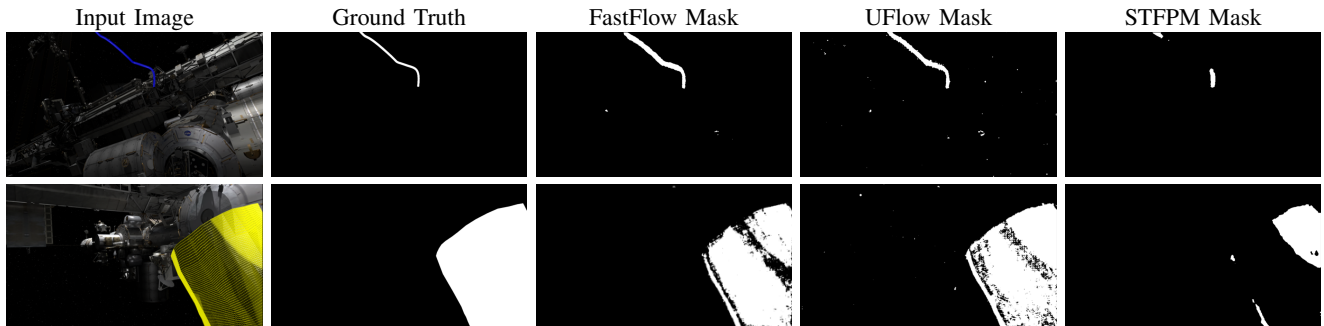


Fig. 7: Example inference from anomaly detection algorithms on colourful anomalies.

Model	LAUROC \uparrow	PAUROC \uparrow	PAP \uparrow
FastFlow [33]	98.8 \pm 0.3	99.4 \pm 0.2	87.9 \pm 0.7
UFlow [26]	97.3 \pm 1.1	98.8 \pm 0.3	91.7 \pm 0.8
Rev. Dist. [21]	94.1 \pm 0.6	96.1 \pm 0.1	74.3 \pm 0.9
STFPM [38]	95.3 \pm 1.5	93.4 \pm 2.3	81.8 \pm 2.9

TABLE IV: Performance of best four anomaly detection algorithms from the benchmark on the secondary colour test set. For each metric, the algorithm that performed best and second-best are bolded and underlined, respectively.

tection algorithms is their assumption of image consistency. The methods evaluated in this benchmark were developed for applications in which images are taken under consistent, monochrome lighting from the same viewpoint (e.g. industrial defect inspection, medical imaging). This means that the anomaly score may be incorrect if there is a misalignment between the normal training images and the testing image [47]. In the space domain, lighting varies greatly based on the position of the Moon, Earth, and Sun, and the camera viewpoints in the ALLO dataset differ due to the variety of operations conducted by Canadarm3. These variations make anomaly detection in the space domain a challenging

problem and existing algorithms cannot be directly applied to this task with much success.

V. CONCLUSION

In this paper, we addressed the task of visual anomaly detection and localization for a space station in lunar orbit, a previously unexplored area that is extremely valuable for autonomous space operations. The varying lighting conditions and complex scene geometry of space imagery must be addressed before an algorithm can be deployed on a space station. To tackle these challenges, we introduce the ALLO dataset and an automated data generation pipeline, marking the first open-source anomaly detection dataset featuring images from lunar orbit. We evaluate state-of-the-art methods on this dataset, establishing a new benchmark to guide future research. We highlight that the similarity between normal and anomalous features in the space domain presents a major challenge for current anomaly detection methods. As autonomy becomes increasingly important in future missions, we aim for this dataset and data generation pipeline to be foundational in developing robust anomaly detection algorithms for space exploration.

REFERENCES

- [1] J. C. Crusan, R. M. Smith, D. A. Craig, J. M. Caram, J. Guidi, M. Gates, J. M. Krezel, and N. B. Herrmann, "Deep space gateway concept: Extending human presence into cislunar space," in *2018 IEEE Aerospace Conference*, pp. 1–10. [Online]. Available: <https://ieeexplore.ieee.org/document/8396541>
- [2] NASA's gateway program - NASA. Section: Humans in Space. [Online]. Available: <https://www.nasa.gov/reference/nasas-gateway-program/>
- [3] (2020, June) About Canadarm3. [Online]. Available: <https://www.asc-csa.gc.ca/eng/canadarm3/about.asp>
- [4] T. Ehret, A. Davy, J.-M. Morel, and M. Delbracio, "Image anomalies: a review and synthesis of detection methods," vol. 61, no. 5, pp. 710–743. [Online]. Available: <http://arxiv.org/abs/1808.02564>
- [5] M. Pajusalu, I. Iakubivskiy, G. J. Schwarzkopf, O. Knuuttila, T. Väisänen, M. Bühner, H. Teras, G. L. Bonhomme, M. F. Palos, J. Praks, and A. Slavinskis, "SISPO: Space imaging simulator for proximity operations," vol. 17, no. 3, p. e0263882. [Online]. Available: <http://arxiv.org/abs/2105.06771>
- [6] S. Parkes, I. Martin, M. Dunstan, and D. Matthews, "Planet surface simulation with PANGU."
- [7] L. Bingham, J. Kincaid, B. Weno, N. Davis, E. Paddock, and C. Foreman, "Digital lunar exploration sites unreal simulation tool (DUST)," in *2023 IEEE Aerospace Conference*. IEEE, pp. 1–12. [Online]. Available: <https://ieeexplore.ieee.org/document/10115607/>
- [8] E. Z. Crues, P. Bielski, E. Paddock, C. Foreman, B. Bell, C. Raymond, T. Hunt, and D. Bulikhov, "Approaches for validation of lighting environments in realtime lunar south pole simulations," in *2023 IEEE Aerospace Conference*, pp. 1–18, ISSN: 1095-323X.
- [9] R. Brochard, J. Lebreton, C. Robin, K. Kanani, G. Jonniaux, A. Masson, N. Despré, and A. Berjaoui, "Scientific image rendering for space scenes with the SurRender software." [Online]. Available: <http://arxiv.org/abs/1810.01423>
- [10] R. T. Eapen, R. R. Bhaskara, and M. Majji, "NaRPA: Navigation and rendering pipeline for astronauts." [Online]. Available: <http://arxiv.org/abs/2211.01566>
- [11] B. Foundation. blender.org - home of the blender project - free and open 3d creation software. [Online]. Available: <https://www.blender.org/>
- [12] Unreal engine 5. [Online]. Available: <https://www.unrealengine.com/en-US/unreal-engine-5>
- [13] P. Bergmann, M. Fauser, D. Sattlegger, and C. Steger, "MVTec AD — a comprehensive real-world dataset for unsupervised anomaly detection," in *2019 IEEE/CVF Conference on Computer Vision and Pattern Recognition (CVPR)*, pp. 9584–9592, ISSN: 2575-7075. [Online]. Available: <https://ieeexplore.ieee.org/document/8954181>
- [14] Y. Zheng, X. Wang, Y. Qi, W. Li, and L. Wu, "Benchmarking unsupervised anomaly detection and localization," publication Title: arXiv e-prints ADS Bibcode: 2022arXiv220514852Z. [Online]. Available: <https://ui.adsabs.harvard.edu/abs/2022arXiv220514852Z>
- [15] MyNew, "Btech dataset," <https://universe.roboflow.com/mynew/btech>, feb 2024, visited on 2024-09-11. [Online]. Available: <https://universe.roboflow.com/mynew/btech>
- [16] D. Tabernik, S. Šela, J. Skvarč, and D. Škočaj, "Segmentation-Based Deep-Learning Approach for Surface-Defect Detection," *Journal of Intelligent Manufacturing*, May 2019.
- [17] K. G. Mehrotra, C. K. Mohan, and H. Huang, *Anomaly Detection Principles and Algorithms*, ser. Terrorism, Security, and Computation. Springer International Publishing. [Online]. Available: <http://link.springer.com/10.1007/978-3-319-67526-8>
- [18] T. M. Tran, T. N. Vu, N. D. Vo, T. V. Nguyen, and K. Nguyen, "Anomaly analysis in images and videos: A comprehensive review," vol. 55, no. 7, pp. 148:1–148:37. [Online]. Available: <https://dl.acm.org/doi/10.1145/3544014>
- [19] G. Pang, C. Shen, L. Cao, and A. v. d. Hengel, "Deep learning for anomaly detection: A review," vol. 54, no. 2, pp. 1–38. [Online]. Available: <http://arxiv.org/abs/2007.02500>
- [20] T. Defard, A. Setkov, A. Loesch, and R. Audigier, "PaDiM: a patch distribution modeling framework for anomaly detection and localization." [Online]. Available: <http://arxiv.org/abs/2011.08785>
- [21] H. Deng and X. Li, "Anomaly detection via reverse distillation from one-class embedding." [Online]. Available: <http://arxiv.org/abs/2201.10703>
- [22] S. Lee, S. Lee, and B. C. Song, "CFA: Coupled-hypersphere-based feature adaptation for target-oriented anomaly localization." [Online]. Available: <http://arxiv.org/abs/2206.04325>
- [23] V. Zavrtanik, M. Kristan, and D. Škočaj, "DRAEM – a discriminatively trained reconstruction embedding for surface anomaly detection." [Online]. Available: <http://arxiv.org/abs/2108.07610>
- [24] C.-L. Li, K. Sohn, J. Yoon, and T. Pfister, "CutPaste: Self-supervised learning for anomaly detection and localization." [Online]. Available: <http://arxiv.org/abs/2104.04015>
- [25] M. Tailanian, P. Muse, and A. Pardo, "A multi-scale a contrario method for unsupervised image anomaly detection." [Online]. Available: <http://arxiv.org/abs/2110.02407>
- [26] M. Tailanian, A. Pardo, and P. Muse, "U-flow: A u-shaped normalizing flow for anomaly detection with unsupervised threshold." vol. 66, no. 4, pp. 678–696. [Online]. Available: <https://doi.org/10.1007/s10851-024-01193-y>
- [27] K. Roth, L. Pemula, J. Zepeda, B. Schölkopf, T. Brox, and P. Gehler, "Towards total recall in industrial anomaly detection." [Online]. Available: <http://arxiv.org/abs/2106.08265>
- [28] N. A. Ahuja, I. Ndiour, T. Kalyanpur, and O. Tickoo, "Probabilistic modeling of deep features for out-of-distribution and adversarial detection." [Online]. Available: <http://arxiv.org/abs/1909.11786>
- [29] E. D. Cook, M.-A. Lavoie, and S. L. Waslander, "Feature density estimation for out-of-distribution detection via normalizing flows," *Proceedings of the Conference on Robots and Vision*, February 2024. [Online]. Available: <https://crv.pubpub.org/pub/3rxx60zs/release/1>
- [30] N. Marchal, C. Moraldo, H. Blum, R. Siegwart, C. Cadena, and A. Gawel, "Learning densities in feature space for reliable segmentation of indoor scenes," vol. 5, no. 2, pp. 1032–1038, conference Name: IEEE Robotics and Automation Letters. [Online]. Available: <https://ieeexplore.ieee.org/document/8962043>
- [31] H. Zhang, Z. Wang, Z. Wu, and Y.-G. Jiang, "DiffusionAD: Norm-guided one-step denoising diffusion for anomaly detection." [Online]. Available: <http://arxiv.org/abs/2303.08730>
- [32] D. Gudovskiy, S. Ishizaka, and K. Kozuka, "CFLOW-AD: Real-time unsupervised anomaly detection with localization via conditional normalizing flows." [Online]. Available: <http://arxiv.org/abs/2107.12571>
- [33] J. Yu, Y. Zheng, X. Wang, W. Li, Y. Wu, R. Zhao, and L. Wu, "FastFlow: Unsupervised anomaly detection and localization via 2d normalizing flows." [Online]. Available: <http://arxiv.org/abs/2111.07677>
- [34] S. Akcay, A. Atapour-Abarghouei, and T. P. Breckon, "GANomaly: Semi-supervised anomaly detection via adversarial training." [Online]. Available: <http://arxiv.org/abs/1805.06725>
- [35] T. Schlegl, P. Seeböck, S. Waldstein, G. Langs, and U. Schmidt-Erfurth, "f-AnoGAN: Fast unsupervised anomaly detection with generative adversarial networks," vol. 54.
- [36] A.-S. Collin and C. De Vleeschouwer, "Improved anomaly detection by training an autoencoder with skip connections on images corrupted with stain-shaped noise," in *2020 25th International Conference on Pattern Recognition (ICPR)*, pp. 7915–7922, ISSN: 1051-4651. [Online]. Available: <https://ieeexplore.ieee.org/abstract/document/9412842>
- [37] A. Bauer, S. Nakajima, and K.-R. Müller, "Self-supervised training with autoencoders for visual anomaly detection." [Online]. Available: <http://arxiv.org/abs/2206.11723>
- [38] G. Wang, S. Han, E. Ding, and D. Huang, "Student-teacher feature pyramid matching for anomaly detection." [Online]. Available: <http://arxiv.org/abs/2103.04257>
- [39] M. Sabokrou, M. Khalooei, M. Fathy, and E. Adeli, "Adversarially learned one-class classifier for novelty detection." [Online]. Available: <http://arxiv.org/abs/1802.09088>
- [40] V. Zavrtanik, M. Kristan, and D. Škočaj, "DSR – a dual subspace re-projection network for surface anomaly detection," in *Computer Vision – ECCV 2022*, ser. Lecture Notes in Computer Science, S. Avidan, G. Brostow, M. Cissé, G. M. Farinella, and T. Hassner, Eds. Springer Nature Switzerland, pp. 539–554.
- [41] International space station 3d model - NASA science. [Online]. Available: <https://science.nasa.gov/resource/international-space-station-3d-model/>
- [42] D. E. Lee, "White paper: Gateway destination orbit model: A continuous 15 year NRHO reference trajectory," NTRS Author Affiliations: NASA Johnson Space Center NTRS Report/Patent Number: JSC-E-DAA-TN72594 NTRS Document ID: 20190030294

- NTRS Research Center: Johnson Space Center (JSC). [Online]. Available: <https://ntrs.nasa.gov/citations/20190030294>
- [43] ASCL.net - skyfield: High precision research-grade positions for planets and earth satellites generator. [Online]. Available: <https://ascl.net/1907.024>
- [44] Z. Wang, A. Bovik, H. Sheikh, and E. Simoncelli, "Image quality assessment: from error visibility to structural similarity," vol. 13, no. 4, pp. 600–612, conference Name: IEEE Transactions on Image Processing. [Online]. Available: <https://ieeexplore.ieee.org/document/1284395>
- [45] S. Akcay, D. Ameln, A. Vaidya, B. Lakshmanan, N. Ahuja, and U. Genc, "Anomalib: A deep learning library for anomaly detection." [Online]. Available: <http://arxiv.org/abs/2202.08341>
- [46] A. Krizhevsky, I. Sutskever, and G. E. Hinton, "ImageNet classification with deep convolutional neural networks," in *Advances in Neural Information Processing Systems*, vol. 25. Curran Associates, Inc., 2012. [Online]. Available: <https://proceedings.neurips.cc/paper/2012/hash/c399862d3b9d6b76c8436e924a68c45b-Abstract.html>
- [47] J. Jang, E. Hwang, and S.-H. Park, "N-pad : Neighboring pixel-based industrial anomaly detection." [Online]. Available: <http://arxiv.org/abs/2210.08768>